Design of 3D printed quasi-2D Metamaterials for Waveguiding

Bachelor Integration project:

Industrial Engineering and Management

June 23, 2025

Author:
Minke Westra (s5323096)

Supervisor:
prof. dr. A.O. Krushynska

Daily supervisor:
S. Beniwal

Second assessor:
M. Mohebbi

Abstract

Metamaterials are artificially engineered materials that can control wave propagation. Applications such as energy harvesting or signal processing require waves to be guided to certain locations with minimal energy losses. This work presents two quasi-2D metamaterial designs for waveguiding. Both designs consist of circular unit cells with four connecting ligaments, arranged in a seven-by-seven square. The structures are fabricated using fused deposition modelling (FDM) 3D printing. Based on the results of parametric studies, arrangements of unit cell configurations are chosen to enable precise waveguiding. The first design effectively confines waves along the outer rim in the frequency ranges 6.9-9.2 kHz, 15.7-16.1 kHz, and 16.3-16.7 kHz. The other metamaterial design localises waves along a predefined straight path in the frequency ranges 6.2–8.2 kHz, 8.8–9.3 kHz, and 13.7–14.8 kHz. The numerical viscoelastic model of the structures in COMSOL Multiphysics accurately predicted the transmission behaviour observed in the experiments.

Table of Contents

Chapter 1 Introduction

Elastic metamaterials are engineered materials that can control wave propagation in a desired manner [1]. Metamaterials have precisely designed geometries and (usually) exhibit periodicity [2]. Especially noteworthy is the ability of metamaterials to attenuate waves with larger wavelengths than the dimensions of their repetitive unit, from now on referred to as the unit cell [3] [4]. Such waves can be controlled through local resonances within metamaterials [5]. The architecture of the unit cells predominantly dictates wave propagation in metamaterials [6], which employs three fundamental physical mechanisms: Bragg scattering, local resonance, and inertial amplification [7] [8].

Applications of metamaterials span numerous interesting possibilities across a wide range of disciplines. Metamaterials have been studied in the field of acoustics [9], civil engineering, and mechanics, to name a few [10]. One highlighted emerging application is energy harvesting from metamaterials as a potential renewable energy strategy. The working principle is that kinetic energy from vibration in the metamaterial can be converted to electrical energy to power electronic devices with low consumption [5]. Energy harvesting can even be combined with vibration suppression applications, such as noise control. Noise or other unused mechanical vibration then serves as the vibration source. Piezoelectric materials are often utilised for efficient energy conversion. Metamaterials enable waveguiding and can therefore achieve a higher energy harvesting efficiency than conventional devices [11] [12] [13]. Waveguiding can be utilised for more applications such as sensors and digital logic circuits [7].

This study aims to design two quasi-2D metamaterials, manufactured by 3D printing, that experimentally realise waveguiding. Both designs consist of circular unit cells with four connecting ligaments. One metamaterial is designed to confine waves along the outer rim of unit cells, while the other aims to guide waves along a straight path.

The report is structured as follows. The next chapter introduces the research context, highlighting the design of the unit cell that will be studied (Chapter 2). Afterwards, the theoretical background on bandgaps and waveguiding relevant to this study is discussed (Chapter 3). Chapter 4 shortly discusses 3D printing and the material that is utilised. Then, Chapter 5 explains the parametric analysis and discusses its results. From the results of the parametric analysis, the metamaterial designs are presented in Chapter 6. Subsequently, the numerical and experimental results from the transmission analysis are discussed, and the effectiveness of the metamaterials is analysed. (Chapter 7). The last chapter presents the conclusion and identifies possibilities for future studies (Chapter 8). The report concludes with a list of references followed by the appendices.

Chapter 2 Research context

The metamaterial that has been studied before is a quasi-1D structure (Figure 2.1). The structure has circular unit cells with two connecting ligaments. The unit cells are placed next to each other along one axis, creating a periodic structure. This research aims to create the quasi-2D counterpart of the quasi-1D structure that can be 3D printed. The metamaterial designs for waveguiding will have nonidentical topologically equivalent unit cells arranged in a 2D plane.

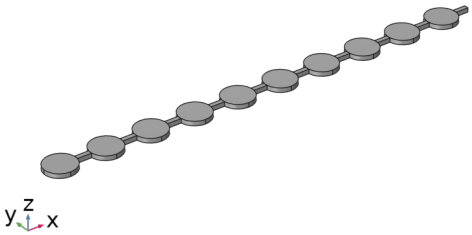

Figure 2.1: Isometric view of quasi-1D metamaterial with circular unit cells and connecting ligaments [14].

The out-of-plane direction in this research is the z-direction, while the x and y-direction are in-plane directions. Therefore, out-of-plane wave propagation entails the propagation and thus displacement along the z-axis. In the 2D metamaterial, the unit cells will be placed along both the x- and the y-axis. The unit cell for a 2D structure requires connecting ligaments on four sides. Figure 2.2 presents the unit cell and its parameters. The thickness of the unit cell remains constant at $t_{fixed} = 4.0$ mm over the entirety of this study, as only the design parameters in the 2D plane are considered.

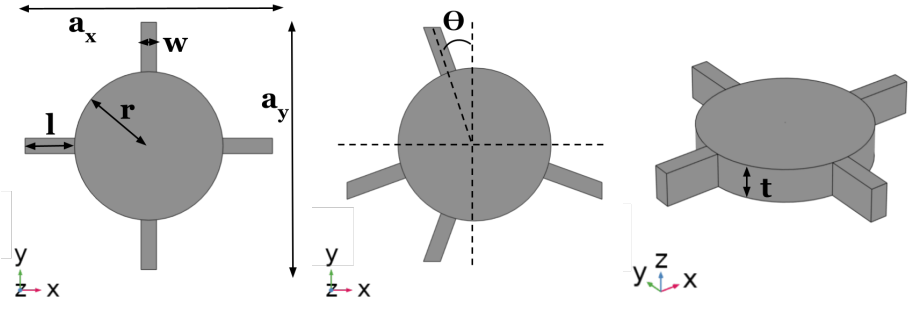

(a) *(b)* *(c)*

Figure 2.2: Circular unit cell with four connecting ligaments (a) in XY-plane view, (b) with non-zero inclination angle in XY-plane view, and (c) in isometric view. The figures show five parameters that define the unit cell: the radius of the circle (r), the width of the ligaments (w), the length of the ligaments (l), the inclination angle of the ligaments (θ), and the thickness of the entire structure (t). Additionally, the overall unit cell size in the x-direction (a_x) and the y-direction (a_y) are indicated.

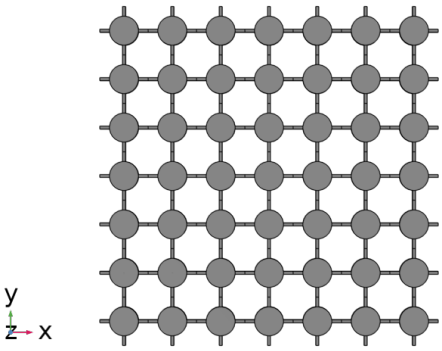

Figure 2.3: Illustration of 2D metamaterial with circular unit cells arranged in a seven-by-seven square.

The unit cell size (a_x) will remain fixed at 32.0 mm for the final designs in this research. The size of 32.0 mm ensures that seven unit cells can be manufactured reliably in x- and y-direction with the 3D printer. The two metamaterial designs will both consist of 49 unit cells, arranged as illustrated in Figure 2.3. Furthermore, a_y is equal to a_x, because the unit cell has the same size in the x- and y-direction. From now on, this research refers to the unit cell size as a, which is not different from a_x and a_y. The consequence of fixing a is that a dependency between length (l) and the radius (r) occurs. Therefore, w, r, and θ are the independent design parameters considered in this research.

Chapter 3 Theory

Wave control and, therefore, waveguiding in a metamaterial depend on its geometric structure. The shape and arrangement of the unit cells in the metamaterial define the bandgaps.

3.1 Bandgaps

A bandgap is a frequency range in which wave propagation is blocked [15]. Researchers are particularly interested in bandgaps at low frequencies, which are convenient for various applications [16]. The desired bandgaps and therewith controlled wave propagation can be achieved by tuning the design parameters of the unit cells [6]. In this research, only the out-of-plane bandgaps are considered, mainly because the quasi-2D metamaterials can experimentally only be tested for out-of-plane wave propagation.

Bandgaps in a (quasi-2D) periodic metamaterial can be identified by studying the wave numbers from the first Brillouin zone. The first Brillouin zone is defined by the reciprocal lattice. The irreducible Brillouin zone is the smallest part of the first Brillouin zone that, due to symmetry, can fully characterise the dispersion of the metamaterial. The grey area in Figure 3.1 highlights the irreducible Brillouin zone. In a 2D structure, three directions define the irreducible Brillouin zone: Γ-X, X-M, and Γ-M. Studying these three directions can fully characterise the dispersion and thus the bandgaps of a 2D metamaterial [7] [17]. The unit cell considered in this study is symmetric along the x- and the y-direction ($a_x = a_y$). Therefore, it suffices to study only the dispersion in Γ-X and Γ-M direction to characterise the wave propagation in the unit cell.

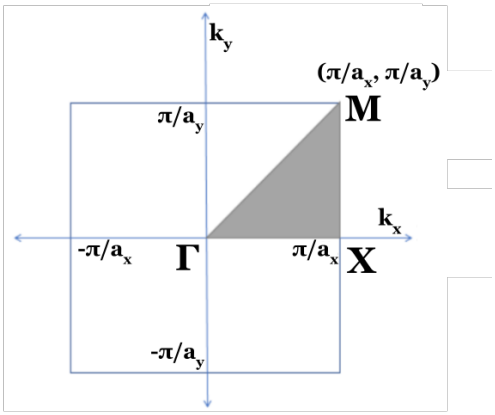

Figure 3.1: Schematic of the Brillouin zone for a periodic 2D geometry. The wavevectors in x- and y-direction are denoted by k_x and k_y, respectively. Adapted from [17].

3.1.1 Bragg scattering

Bandgaps can occur because of several phenomena, of which three are discussed in this section. In metamaterials, bandgaps form through Bragg scattering of (acoustic) waves. The spatial periodicity of the impedance mismatch leads to Bragg scattering. Bragg bandgaps occur because of the destructive interference of the scattered waves from neighbouring repeated structural

elements, which are the circular part and the ligaments in this research. Bragg bandgaps mostly occur at short wavelengths, in the order of the size of the unit cell [18] [19] [20]. Bragg bandgaps are often easily recognisable by a smooth and often broad curve in transmission curves, which plot the transmission (in dB) against the frequency. Bragg bandgaps are often wide because they form from scattering due to periodicity. Additionally, besides destructive interference, partial destructive interference can also form bandgaps [7].

3.1.2 Local resonance

Bandgaps from local resonance in metamaterials occur because of the resonant frequency of the structural elements. Locally resonant metamaterials often consist of high mass density parts supported by highly compliant parts. This ensures strongly localised vibrations in the parts with a high mass density at the resonant frequency. Local resonance bandgaps form because of the strong coupling of the localised vibration modes. In the metamaterial in this study, the circular parts have the highest mass density, and the connecting ligaments can have a low stiffness. The width of the ligaments (w) is the independent parameter that governs the stiffness of the ligaments. The radius (r) governs the mass of the circle. Therefore, these two parameters influence the formation of bandgaps through local resonance. Bandgaps formed by local resonances are independent of the periodicity of the metamaterial. Therefore, locally resonant metamaterials can form bandgaps at long wavelengths and thus low frequencies. However, large masses and/or low stiffness are required for bandgaps in a low frequency range. As opposed to Bragg scattering, local resonance bandgaps are often recognised by steep, narrower transmission peaks [7] [21].

3.1.3 Inertial amplification

Inertial amplification is the last mechanism that can generate bandgaps in metamaterials. Inertial amplification can, for example, be achieved by inclining parts of the unit cell or by introducing a rotational degree of freedom. With this mechanism, the overall inertia of the metamaterial can be amplified by decreasing its resonant frequency. Therefore, lower and wider bandgaps than those from local resonances can be achieved. In this research, inclining the ligaments enables inertial amplification in the metamaterial. Therefore, the independent design parameter θ, the ligament inclination angle, influences bandgaps generated from inertial amplification [8] [16].

3.2 Waveguiding

A metamaterial is effective for waveguiding if the structure can ‘guide’ the waves along a predefined path with minimal energy dissipation. Waveguiding is realised, for example, by introducing ‘defects’ into the metamaterial. This entails that part of the structure has a different configuration. In this study, a defected region entails that the metamaterials consist of nonidentical topologically equivalent unit cells. The defected unit cells have one or more modified design parameters compared to the unit cells in the rest of the structure. Therefore, the unit cells along the path have different bandgaps from the rest of the structure. Within the bandgap frequency of the rest of the structure, waves can only propagate along the path of defected unit cells. In other words, the waves are confined to or localised at a predefined defect path [2] [7] [11].

Chapter 4 3D printing and material

The metamaterial designs were manufactured with 3D printing and more specifically with Fused Deposition Modelling (FDM) [14] [22], using Bambu Lab X1 Carbon 3D printers, equipped with a 0.4 mm nozzle. Consequently, all design parameters should be selected as integer multiples of 0.4 mm to ensure the sample can be printed [23]. Additionally, other printing constraints should be considered for the metamaterial design. For example, printing a ligament as a single layer does not provide sufficient strength to the sample.

The material that was used for 3D printing is Polylactic acid (PLA). Temperature variations cause negligible shrinking in PLA printed parts. Additionally, PLA is made from renewable resources and is often completely biodegradable [24]. The material properties of the specific PLA filament used for this study are listed in Table 4.1. The material properties were characterised with the methods described in [14].

Material property	**Value**
Young's modulus (E)	$1.720 \cdot 10^9$ Pa
Shear storage modulus (G_1)	$7.174 \cdot 10^8$ Pa
Shear loss modulus (G_2)	$2.366 \cdot 10^7$ Pa
Poisson's ratio (ν)	0.3459
Density (ρ)	1144 kg/m^3

Table 4.1: Material properties of PLA filament used for 3D printing.

Chapter 5 Parametric analysis

The influence of the three geometric parameters (w, r, and θ) on the out-of-plane bandgaps is studied to design a metamaterial for waveguiding. To conduct the parametric studies, the unit cell defined in Chapter 2 is modelled in the software COMSOL Multiphysics. The periodic Floquet boundary conditions are applied to the four lateral faces of the unit cell, such that an infinite quasi-2D plane metamaterial is simulated [25]. A parametric sweep is conducted for each of the three independent design parameters. The simulation for each parameter sweeps over the respective design parameter and the wavenumbers simultaneously. The wavenumbers are varied in the irreducible Brillouin zone. In Γ-X direction k_x ranges from 0 to $\frac{\pi}{a}$ and $k_y = 0$ for every configuration of the parameter. In Γ-M direction both k_x and k_y range from 0 to $\frac{\pi}{a}$ [3] [7] [17]. The number of steps is set to thirty for the wavenumbers. For all configurations of the respective parameter and the wavenumbers, the first fifteen eigenfrequencies are calculated by the finite element method using the Solid Mechanics Module in Comsol Multiphysics [2].

$$p = \frac{\int_V |w|^2 dV}{\int_V (|u|^2 + |v|^2 + |w|^2) dV} \tag{5.1}$$

For all eigenfrequencies, the polarisation is calculated with Equation 5.1. Here V is the volume of the unit cell and u, v, and w are the displacements in respectively x-, y-, and z-direction. The equation determines the fraction of total motion energy associated with out-of-plane motion. The value of p ranges from 0 to 1, where 0 indicates full in-plane motion and 1 indicates full out-of-plane motion. A threshold of $p > 0.75$ is selected to filter the out-of-plane eigenfrequencies [2].

Table 5.1 shows the range for the parametric sweep for the three parameters and the fixed values. The fixed values are the values the parameter is set to when the parametric sweep is conducted for another parameter. The fixed values of the width and the radius are the most feasible parameters that obtained the widest bandgaps for the quasi-1D structure. Additionally, the reference design had an inclination angle $0°$. The range for the ligament width starts from a size of 0.4 mm, as this is the smallest printable size. The radius ranges from 4.0 mm to 10.4 mm. For the radius, 10.4 mm is the largest value that would not exceed V_{fixed}, which is discussed in the next paragraph. A maximum value of 10.0 mm is chosen for the width. This ensures that the ligaments do not overlap and that the structure conforms to the volume constraint. The increments for the width and the radius are 0.4 mm, conforming to the printing constraints. The ligament inclination angle ranges from a $0°$ angle to $39°$, with increments of $1°$. With the other fixed parameters, $39°$ is the largest angle that creates a unit cell without overlapping ligaments.

Parameter	***First value***	***Last value***	*Fixed value*
Ligament width (w)	0.4 mm	10.0 mm	2.0 mm
Radius (r)	4.0 mm	10.0 mm	9.6 mm
Ligament inclination angle (θ)	0°	39°	0°

Table 5.1: Ranges of the design parameters for the parametric study.

To fairly compare the results for each unit cell configuration, the volume should be kept constant:

$$V = t(\pi r^2 + 4lw). \tag{5.2}$$

Equation 5.2 presents the equation of the volume of the unit cell with a 0° inclination angle. The reference values for the parameters from Table 5.1 and $a = 32.0$ mm are selected for setting the fixed volume (V_{fixed}). The length (l) therefore is $l = \frac{a-2r}{2} = 6.4$ mm. Therefore, the fixed volume is $V_{fixed} = 1.363 \cdot 10^{-6}\ m^2$.

$$l = \frac{\frac{V_fixed}{t_{fixed}} - \pi r^2}{4w} \tag{5.3}$$

$$a = 2l + 2r \tag{5.4}$$

To keep the volume of the unit cell constant for the zero inclination angle case, the length (l) of the unit cell is adjusted according to equation 5.3. Therefore, a (Equation 5.4) varies for different configurations of the parameters. The parametric study for the inclination angle results in minimal variation in the volume of the unit cell. The volume decreases slightly because the ends of the ligaments are cut off along the x- and y-axis as shown in Figure 5.1. This ensures that the unit cells can be arranged without overlapping ligaments. The maximum inclination angle of 39° results in a volume of $V = 1.338 \cdot 10^{-6}\ m^2$, which is a negligible volume change of 1.8% with respect to V_{fixed}.

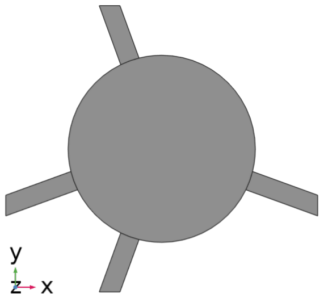

Figure 5.1: Unit cell with 20° inclination angle.

$$a = 0.0320 \cdot cos(\theta) - w \cdot sin(\theta) \tag{5.5}$$

The rotation of the ligaments additionally causes a change in a for the unit cell. The ligaments have a length such that with an 0° angle, $a = 32.0$ mm. The unit cell size when the ligaments are

inclined is calculated with Equation 5.5.

$$\overline{f} = \frac{fa}{c_s} \tag{5.6}$$

$$c_s = \sqrt{\frac{G}{\rho}} = \sqrt{\frac{7.174e8}{1144}} = 791.8951 \text{ m/s} \tag{5.7}$$

Because the unit cell size (a) varies for different configurations of the design parameters, the frequencies should be normalised such that the influence of the parameter can be studied independently from a. The frequencies are normalised with Equation 5.6, in which $\overline{f}$ represents the normalised frequency. The transverse wave speed of sound in PLA is denoted by c_s, which is calculated in Equation 5.7 for the PLA used in this research.

5.1 Ligament width

Condensed band diagrams are calculated for all three design parameters of the unit cell. Figure 5.2 presents the out-of-plane wave propagation ($p > 0.75$) for a varying ligament width. The parametric studies in both Γ-X and Γ-M directions are performed with a fixed radius of 9.6 mm and the ligaments not inclined. In Γ-X direction (Figure 5.2a), it becomes visible that a wide band gap is obtained with small widths, especially in the range below 2.4 mm. The smaller the width, the wider the bandgap. This occurs because the stiffness of the ligaments is of importance to bandgaps from local resonance. Once the ligaments become wider and thus stiffer, the metamaterial does not achieve localised vibration modes. Therefore, a larger width eliminates bandgaps formed through local resonances.

Considering printability, a ligament width of 1.2 mm, 1.6 mm or 2.0 mm is an optimal choice for obtaining a wide bandgap. There are no bandgaps observed from a width above 6.0 mm. In Γ-M direction (Figure 5.2b), the behaviour of the bandgaps is similar. The difference is that in Γ-X, a few bandgaps appear at higher frequencies for small ligament widths. Additionally, a wide bandgap appears up to 6.0 mm in Γ-M direction.

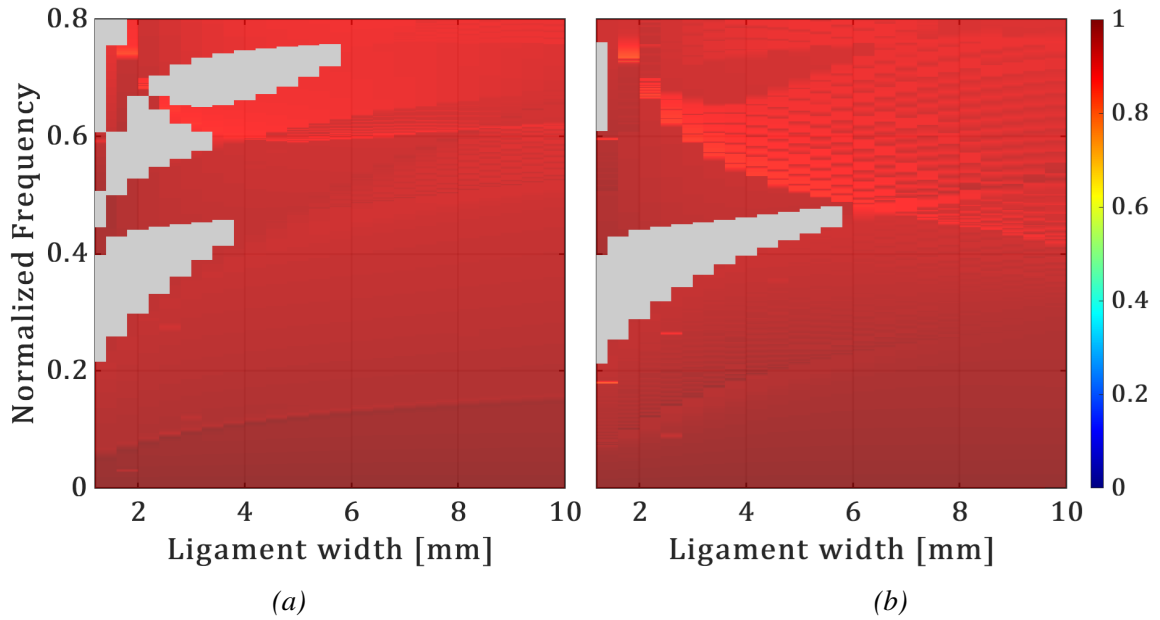

(a) *(b)*

Figure 5.2: Condensed band diagrams for the unit cells with varying ligament width against frequency in (a) Γ-X and (b) Γ-M direction. The out-of-plane bandgaps are shown in grey.

5.2 Circle radius

Figure 5.3 shows the out-of-plane wave propagation ($p > 0.75$) and therefore also the out-of-plane bandgaps of the unit cell for a range of radii. This parametric study is performed with a fixed ligament width of 2.0 mm and an inclination angle of $0°$ for the ligaments. In Γ-X direction (Figure 5.3a), the range of radii below 6.0 mm mainly shows narrow bandgaps. Above a radius of 6.5 mm, the bandgaps become wider. In both directions, the bandgaps become wide starting at a radius of 8.4 mm. In Γ-X direction, both 8.4 and 8.5 mm obtain the widest bandgap. In Γ-M direction (Figure 5.3b), a radius of 10.4 mm obtains the widest bandgap. Comparing the results in both directions highlights that the widest bandgaps are obtained with a radius of 9.6 and 10.0 mm.

In general, the bandgaps become wider as the radius increases. The radius influences the spatial periodicity of the waves in the metamaterial, as the length of the ligaments changes with the radius. Therefore, bandgaps from Bragg scattering appear when the radius changes. Additionally, the mass of the circular element increases with the radius. The stiffness of the ligaments remains constant, and therefore, bandgaps formed through local resonances appear.

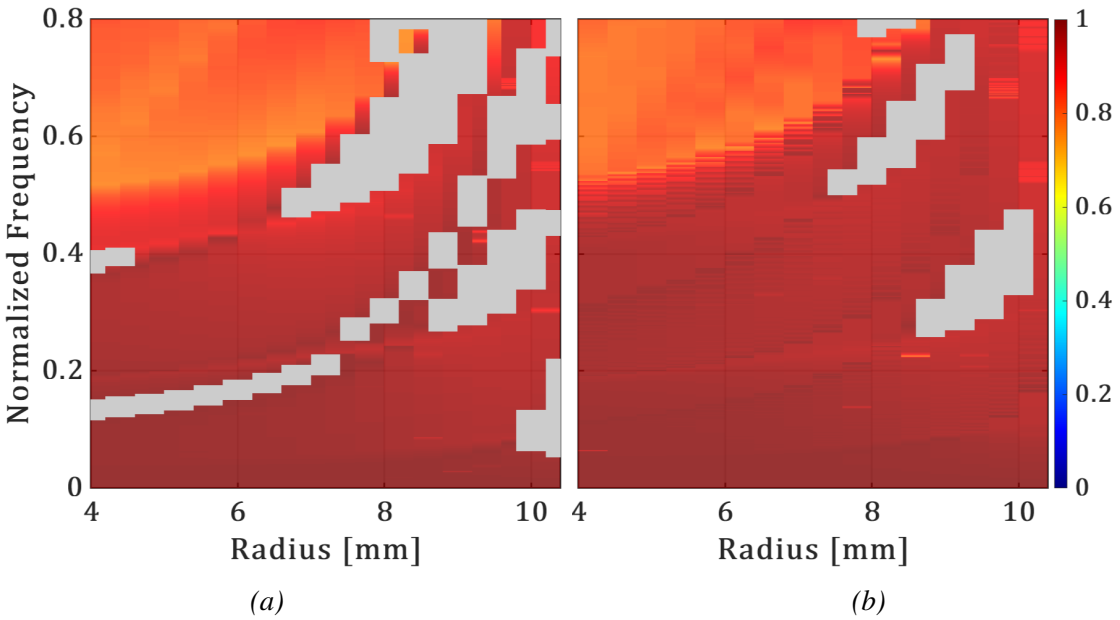

Figure 5.3: Condensed band diagrams for the unit cells with varying circle radius against frequency in (a) Γ-X and (b) Γ-M direction. The out-of-plane bandgaps are shown in grey.

5.3 Ligament inclination angle

Figure 5.4 presents the condensed band diagrams for the ligament angle with a fixed ligament width of 2.0 mm and a fixed radius of 9.6 mm. Only the out-of-plane wave propagation ($p > 0.75$) is plotted, making the out-of-plane bandgaps visible. In Γ-X direction (Figure 5.4a), an inclination angle from $24°$ to $31°$ creates the widest bandgap. In Γ-M direction (Figure 5.4b), the widest bandgap is obtained with an inclination angle of $22°$ or $23°$. Starting at $18°$, two other bandgaps appear, but the bandgap ranging from around 0.2 to 0.4 remains the widest over the entire inclination angle range. The combined results of both directions indicate that an angle of $24°$ would obtain the widest bandgap. Overall, both figures show that the bandgaps are smallest with an inclination angle of $0°$. Differing from the width and radius results, there is no angle for which there are no or solely narrow bandgaps. Overall, it is visible that the inertial amplification mechanism is activated when the ligaments are inclined. Inclining the ligaments widens the bandgaps to a certain point.

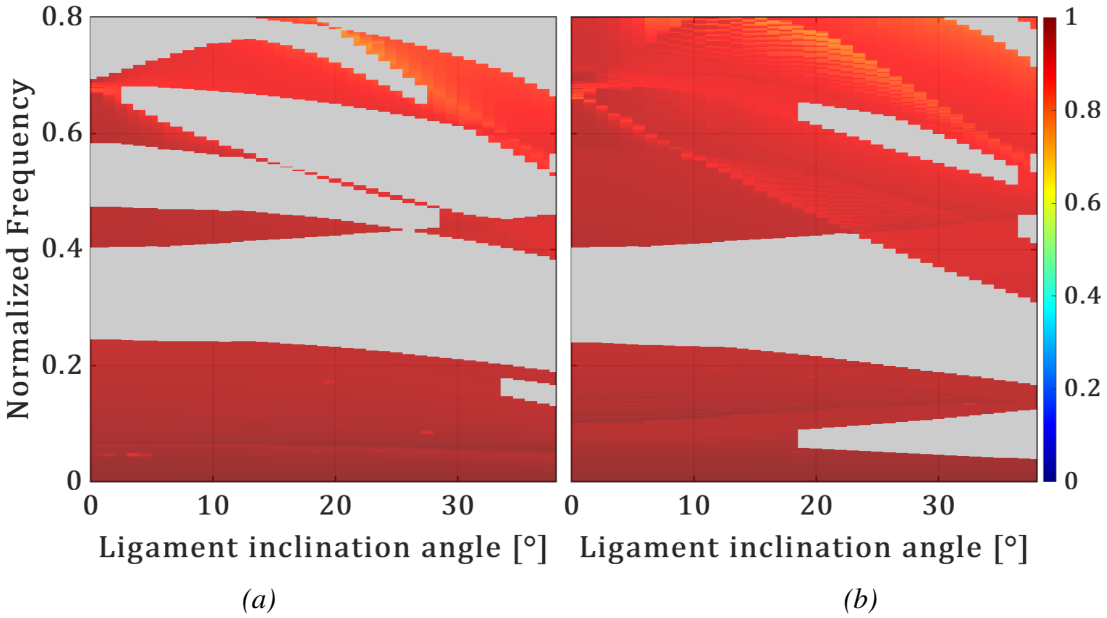

(a) *(b)*

Figure 5.4: Condensed band diagrams for the unit cells with varying ligament inclination angle against frequency in (a) Γ-X and (b) Γ-M direction. The out-of-plane bandgaps are shown in grey.

Chapter 6 Metamaterials design

Based on the parametric analysis, two metamaterials for waveguiding are designed.

$$l = \frac{0.016 + 0.5w \cdot sin(\theta)}{cos(\theta)} - r \tag{6.1}$$

The length of the ligaments for all unit cells in the metamaterial designs is defined by Equation 6.1 to ensure $a = 32.0$ mm. The unit cell volume is thus not kept constant for the metamaterial designs.

Firstly, the design of a metamaterial for waveguiding along the rim is considered. The structure should confine the waves around the outer rim of the metamaterial. Therefore, the metamaterial should be designed such that there is a frequency or frequency range for which waves cannot propagate through the inner part of the metamaterial, while they are not obstructed from propagating along the rim. The inner part should consist of unit cells with a wide bandgap, while the unit cells for the outer rim should not have a bandgap at the same frequency. Firstly, only the influence of the ligament width is considered for designing the metamaterial. Therefore, the radius (r) is 9.6 mm and the inclination angle (θ) is $0°$. A width (w) of 1.2 mm was proven to be a suitable choice for obtaining a wide bandgap while maintaining printability and strength. Figure 6.1a highlights one wide full out-of-plane bandgap for the unit cell with $w = 1.2$ mm. The outer rim will be constructed of unit cells with $w = 8.0$ mm, because the condensed band diagram (Figure 5.2) shows no bandgaps for this width. A lower width is not selected, as that would be close to configurations where a bandgap appears. The dispersion curve for the unit cell with a width (w) of 8.0mm (Appendix A, Figure 1) shows that no full out-of-plane bandgaps appear for this width. Two narrow partial bandgaps in the $\Gamma - X$ direction appear. The lower partial bandgap interferes with the full bandgap of the unit cell with $w = 1.2$ mm. Increasing the ligament width (w) does not significantly influence the interfering bandgap. Therefore, 8.0 mm width (w) is a suitable choice to achieve the goal of the structure, without wasting printing material. The radius is now considered to eliminate the interfering bandgap. With thick ligaments, only increasing the radius from $r = 9.6$ mm preserves the original shape of the unit cell. When a lower radius is chosen, the ligaments start to overlap. The radius study presented in Figure 5.3 goes up to $r = 10.4$ mm, which does not cause a significant difference to the radius or the interfering bandgap. Figure 6.1b shows that a radius of 12.0 mm is a suitable choice. The unit cell has one partial bandgap that does not interfere with the full bandgap in the thin ligament unit cell.

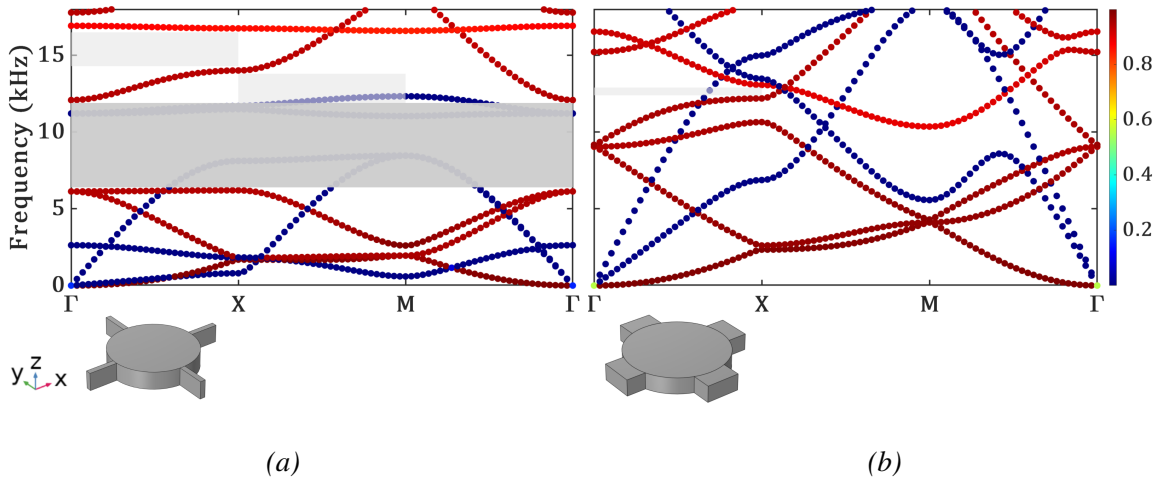

(a) *(b)*

Figure 6.1: Dispersion curves for the configurations (a) $w = 1.2$ mm, $r = 9.6$ mm, and $\theta = 0°$ and (b) $w = 8.0$ mm, $r = 12.0$ mm, and $\theta = 0°$. The colours indicate the direction of wave propagation, ranging from in-plane (blue) to out-of-plane (red). The full out-of-plane bandgaps are highlighted in dark grey. The light grey areas indicate partial out-of-plane bandgaps.

The second design is a metamaterial for waveguiding along a predefined, straight path. For waveguiding in a certain frequency range, the waves should be obstructed from moving anywhere besides the path. Therefore, the unit cells outside the path should have one or more wide bandgaps. Ideally, the unit cells along the path do not have any bandgaps. The influence of the unit cell radius (r) is not considered in the design of this metamaterial, and therefore $r = 9.6$ mm for the entire structure. With this radius and a thickness of 2.0 mm, a $24°$ inclination angle obtains the widest bandgap, which is suitable for the design outside the path. Considering a structure with inclined ligaments, a thinner ligament is avoided to preserve the strength of the ligaments despite the potential for a wider bandgap. The dispersion curve for the unit cell with a $24°$ inclination angle is presented in Figure 6.2a. The graph shows three full bandgaps at the frequency ranges of 6.3-9.5 kHz, 10.5-12.6 kHz, and 14.4-16.6 kHz. A unit cell without an inclination angle of $0°$ and thick ligaments is the most suitable configuration for full wave propagation over a wide frequency range. To achieve waveguiding along the rim, a width of 8.0 mm was chosen. Increasing the width to 10.0 mm compresses the partial bandgap between 10.0 and 15.0 kHz, which interferes with the full bandgaps of the inclined unit cell (Figure 6.2b). Therefore, a ligament width of 10.0 mm is chosen for the path.

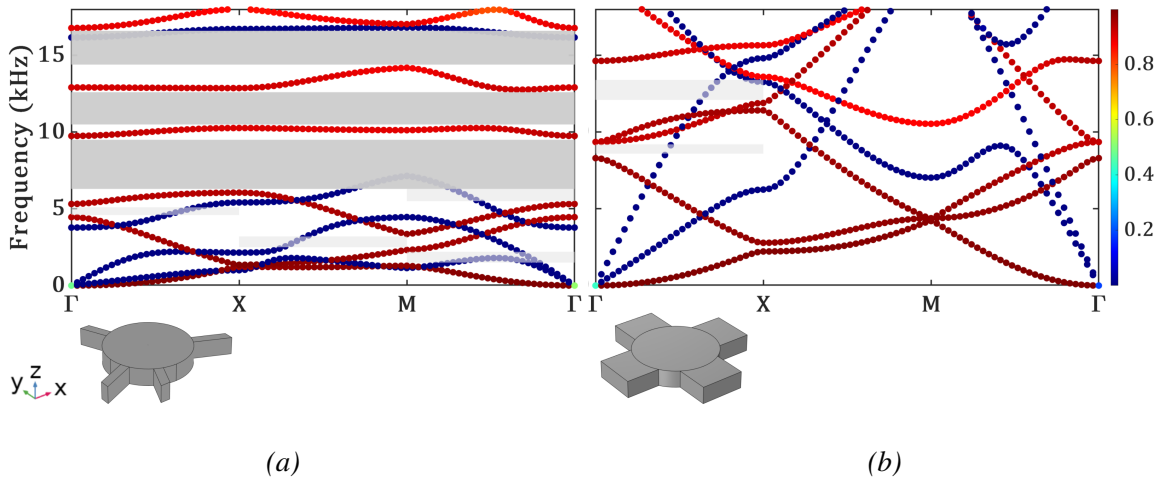

(a) *(b)*

Figure 6.2: Dispersion curves for the configurations (a) $w = 2.0$ mm, $r = 9.6$ mm, and $\theta = 24°$ and (b) $w = 10.0$ mm, $r = 9.6$ mm, and $\theta = 0°$. The colours indicate the direction of wave propagation, ranging from in-plane (blue) to out-of-plane (red). The full out-of-plane bandgaps are highlighted in dark grey. The light grey areas indicate partial out-of-plane bandgaps.

The slight deviation between the condensed band diagrams from the parametric analysis in Chapter 5 and the dispersion curves should be discussed. The discrepancy is particularly noticeable in the dispersion curves of unit cells with thick ligaments (Figure 6.1b and 6.2b), where narrow partial bandgaps appear in the Γ–X direction, despite the absence of such bandgaps in the corresponding condensed band diagrams for ligament widths above 6.0 mm. This occurs even when the other design parameters were the same in both cases ($r = 9.6$ mm and $\theta = 0°$). A plausible explanation for this inconsistency lies in the difference in unit cell size. The unit cell volume was kept constant in the parametric analysis, resulting in varying unit cell sizes (a) across configurations. For example, at a ligament width of 10.0 mm, the unit cell length was $a = 21.8$ mm. A fixed unit cell size of $a = 32.0$ mm was used for the dispersion curves and final metamaterial designs. The difference of $\left(\frac{32-21.8}{32}\right) \cdot 100\% \simeq 31.9\%$ can affect wave propagation characteristics. Similarly, deviations from the standard value of 9.6 mm for the circle radius introduce further variation. Increases in the inclination angle up to $39°$ can reduce a as much as 26.3%. Nonetheless, the design decisions based on the condensed band diagrams remain valid, as the frequency values were normalised, rendering the unit cell size (a) dimensionless in the analysis. Therefore, the observed discrepancies between the condensed band diagrams and the dispersion curves are primarily due to geometric effects and do not undermine the qualitative insights derived from the parametric study. A similar explanation applies to the slight frequency shifts observed in some bandgaps of the dispersion curves relative to those in the condensed band diagrams.

Chapter 7 Transmission analysis

The functioning of the metamaterials for waveguiding is tested with transmission analysis. Wave propagation and attenuation were analysed by measuring signal transmission in the metamaterial samples [2]. Firstly, the metamaterials were modelled in COMSOL Multiphysics for numerical transmission analysis. Afterwards, the designs were tested experimentally as well. The experiments were executed by pitch-catch transmission tests with a non-contact laser Doppler vibrometer (LDV) [14]. Figure 7.1 shows the experimental setup. Figure 7.2 gives a more detailed view of the fixation of the metamaterials to the vibrational shaker. The setup eliminates the influence of gravitational forces on the out-of-plane wave propagation. The experimental setup employs a vibrational shaker as a source. The frequency range over which the metamaterials were tested is 0.1-18.0 kHz, since the shaker cannot go much higher than 18.0 kHz. Via the amplifier, the shaker induces vibration in the sample at the specified frequency. Reflective tape is pasted to the unit cells where the signal should be detected. The LDV is first used to acquire the signal at the vibration source, i.e., the unit cell connected to the shaker. This data is used as a reference and ensures the reliable performance of the setup. Afterwards, the LDV is used to measure the acquisition at the desired unit cell. The data was processed in MATLAB to generate transmission curves [14].

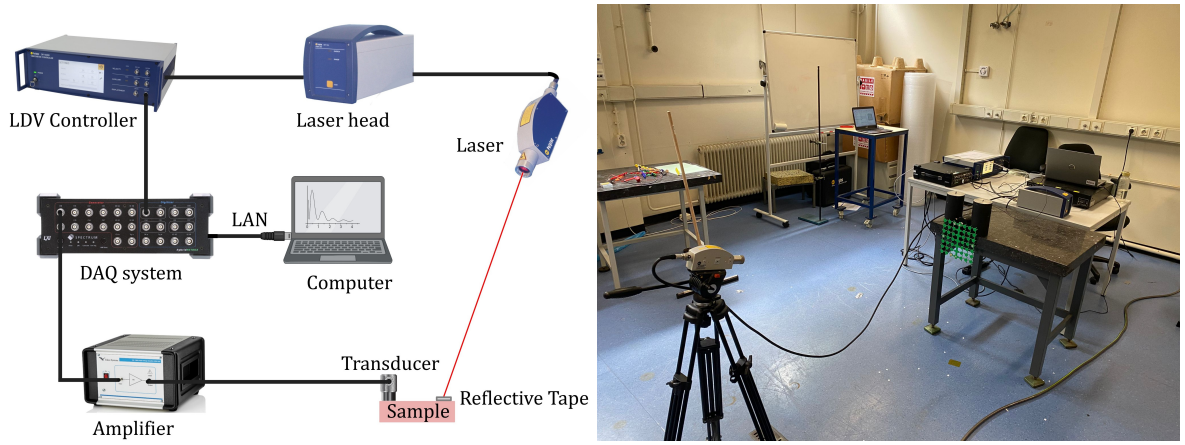

(a) *(b)*

Figure 7.1: (a) Schematic representation adapted from [14] and (b) picture of pitch-catch transmission experiment. The testing setup for pitch-catch transmission tests with a non-contact LDV.

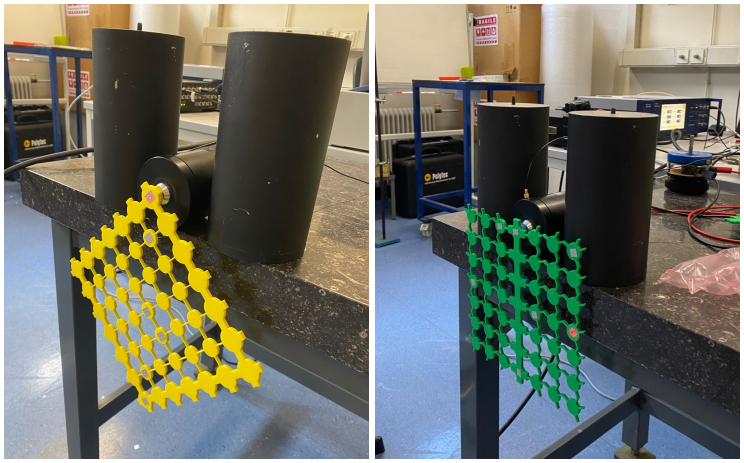

(a) *(b)*

Figure 7.2: Metamaterial samples attached to the vibrational shaker for the experiments.

The metamaterial samples are connected to the shaker by a 3D-printed disc to which a screw is attached. This connector to the source is also modelled in COMSOL Multiphysics for the transmission simulations (Figure 7.3).

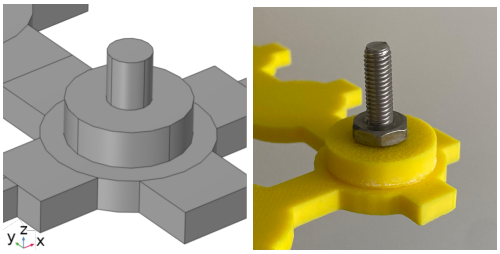

(a) *(b)*

Figure 7.3: (a) The COMSOL multiphysics model and (b) the 3D-printed version of the connector to the source.

The numerical transmission analysis was performed with a viscoelastic model of the metamaterial samples in the frequency domain [2].

$$t = 20 \log_{10} \left(\frac{d_z}{d} \right) \tag{7.1}$$

The transmission (t) in decibels (dB) is calculated with Equation 7.1, in which d_z is the amplitude of displacement in the z-direction at the output and d is the amplitude of displacement at the excitation source. An input excitation of 10^{-6} m is applied to the modeled screw, representing the experimental excitation condition. The transmission is calculated at a square in the middle of the desired unit cell, representing the reflective tape of the experimental setup. Figure 7.4 and 7.11 highlight the places of excitation and acquisition in the following sections. The numerical data was also processed in MATLAB to generate transmission curves.

7.1 Waveguiding outer rim

Figure 7.4 presents the designed metamaterial for waveguiding along the rim. The rim, except for the corners, consists of unit cells with three 8.0 mm thick ligaments and one thin ligament. This design ensures a consistent connection to the middle and a clear distinction of the rim. The middle fully consists of unit cells with the thin ligament configuration. Appendix C Figure 2 and 3 presents numerical transmission results for an alternative configuration of the metamaterial design for waveguiding along the rim. The results clearly show that waveguiding is less evident in this structure, compared to the one discussed here. Both configurations are given the initial displacement of 10^{-6} m at the unit cell in the left corner. The objective of the metamaterial is to confine the waves along the rim. The transmission is therefore measured at a unit cell on the rim and compared to the transmission of unit cells in the middle. The unit cell in the corner is chosen for transmission measurement on the rim, as this is the furthest away from the excitation point. Therefore, the transmission at the corner unit cell represents waveguiding along the entire rim. Multiple unit cells in the middle of the structure are investigated to examine the symmetry and the effectiveness of the metamaterial.

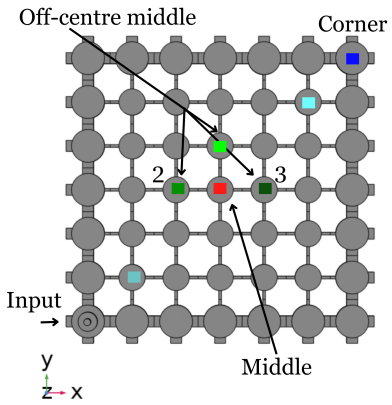

Figure 7.4: The designed metamaterial for waveguiding along the outer rim. The coloured squares indicate the points at which the transmission is measured and correspond with the colours in the transmission curves for this structure.

The metamaterial is designed so that waveguiding is achieved within the bandgap. The full transmission curve in Figure 7.5 shows that from 6.0 kHz the transmission is interesting. Besides the bandgap, the frequency range after 13.0 kHz is notable. Figure 7.6 compares numerical and experimental results in detailed views from 6.0-12.0 kHz and 12.0-18.0 kHz. Figure 7.7 compares the displacement throughout the metamaterial for three different frequencies. The three chosen frequencies correspond to one frequency outside of any (partial) bandgap (4.7 kHz), one in the full bandgap of the thin ligament unit cell (9.1 kHz), and one in a partial bandgap of the thin ligament unit cell (14.9 kHz). Table 1 in Appendix B provides the maximum displacement in the structure at these frequencies.

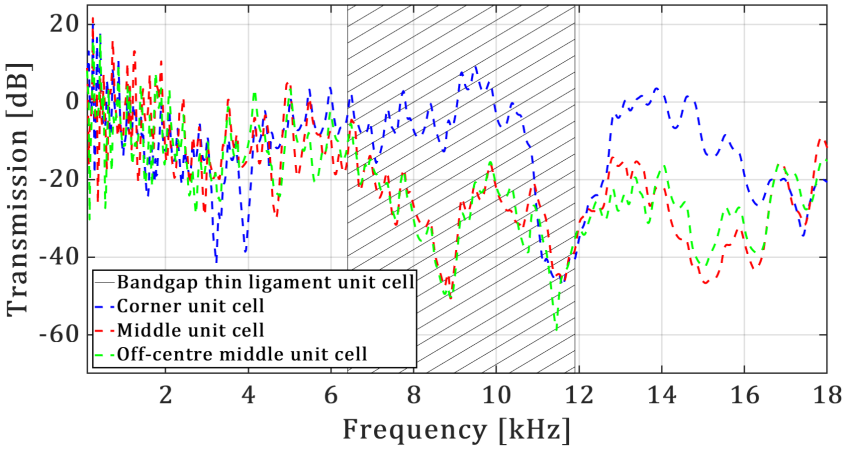

(a)

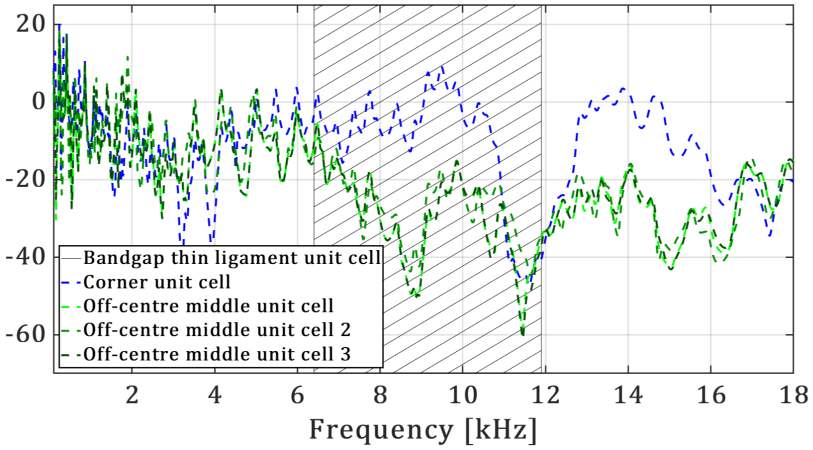

(b)

Figure 7.5: Numerical transmission curve for the entire frequency range from 0.1 to 18 kHz for (a) the corner, middle, and off-centre middle unit cells and (b) the corner and three off-centre middle unit cells. The numerically obtained bandgap of the thin ligament unit cell is indicated by the dashed lines.

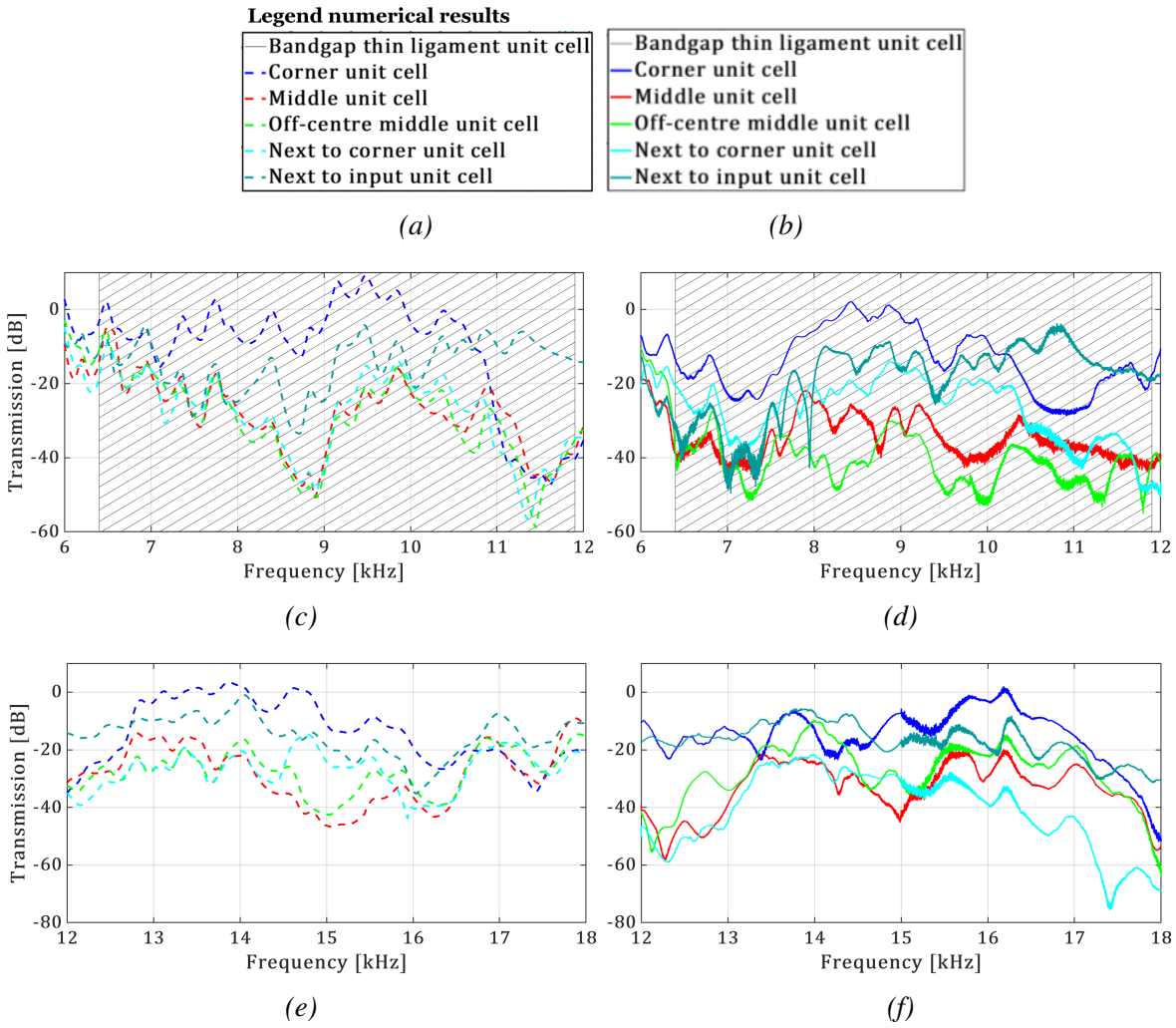

Figure 7.6: Legend for (a) the numerical and (b) the experimental results. Comparison of (c) the numerical transmission curve for 6-12 *kHz, (d) the experimental transmission curve for* 6-12 *kHz, (e) the numerical transmission curve for* 12-18 *kHz, and (f) the experimental transmission curve for* 12-18 *kHz. The numerically obtained bandgap of the thin ligament unit cell is indicated by the dashed lines.*

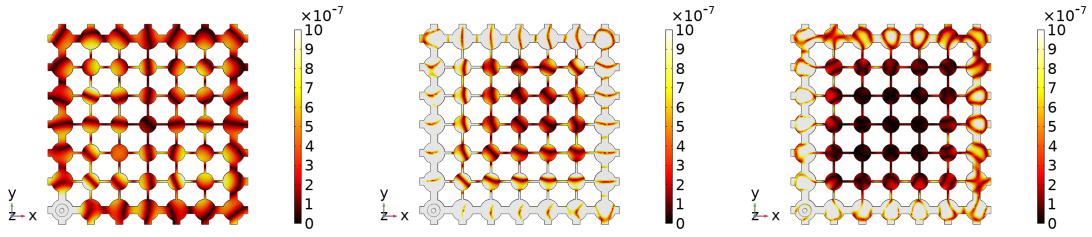

Figure 7.7: Displacement graphs for the waveguiding along the rim metamaterial at (a) 4.7 *kHz, (b)* 9.1 *kHz, and (c)* 14.9 *kHz.*

Numerical comparison of the two unit cells in the middle that are symmetrically positioned with respect to the excitation point reveals that the transmission is almost identical (Figure 7.5b). The

symmetry throughout the structure is also highlighted in the displacement graphs (Figure 7.7). Besides the points close to the line of symmetry, even the symmetrically located points along the rim clearly show symmetry. Experimentally, tests for symmetry have not been conducted.

Comparison of the numerical and experimental results reveals a slight misalignment in the transmission of the middle and the off-centre middle unit cells (Figure 7.6). Numerically, only a slight difference in transmission appears between the middle unit cell and the unit cells that are horizontally or vertically one unit cell from the middle. The results from the experiments reveal that the difference is considerable. However, both the numerical and experimental results show that the overall behaviour of the two unit cells is comparable. Another difference between the numerical and experimental transmission curves comes from the unit cell next to the input. In the numerical graph, the transmission of the unit cell next to the input is lower than that of the corner unit cell from 12.8 to 16.2 kHz. Experimentally, it only holds from 14.8 to 17.4 kHz, which implies the range has shifted and became narrower. The difference is mostly due to the difference in the behaviour of the corner unit cell, as the transmission of the unit cell next to the input overall aligns well.

Overall, the frequency ranges over which there is a significant difference in transmission between the corner unit cell and the others only differ slightly between the numerical and experimental results. The unit cell next to the input is chosen for comparison through this discussion, as this unit cell has the highest overall transmission from all unit cells in the middle. The unit cell next to the input is the best benchmark to conclude successful waveguiding throughout the entire metamaterial. Numerically, a significant difference in transmission of at least 10.0 dB between the corner unit cell and the unit cell next to the input occurs from 7.2 to 10.7 kHz in the bandgap. The transmission difference indicates that waveguiding is achieved in the specified frequency range [2]. Notably, waveguiding occurs in a region smaller than the bandgap predicted by dispersion analysis. Two reasons could explain the behaviour. Firstly, the unit cells on the outer rim of the metamaterial are not completely thick ligament unit cells, which might influence the bandgaps of the thick ligament structure. Additionally, the dispersion analysis has been performed for an infinitely periodic arranged unit cell as opposed to a finite structure. The experimental results show a considerable difference in transmission between 6.9 and 10.1 kHz. Waves are successfully localised along the rim from 6.9 to 9.2 kHz, because a transmission difference of around 10.0 dB is observed. In the specified frequency ranges, the relation of the transmission levels of each unit cell does not significantly vary relative to one another. This behaviour is observed in the numerical and experimental results, indicating that waveguiding along the rim remains uniform throughout the entire frequency range.

Interestingly, the structure also appears to achieve wave confinement in a partial bandgap in Γ-X direction of the thin ligament unit cell (14.3-16.5 kHz) (Figure 7.6e and 7.6f). Waveguiding was not predicted in this region. As discussed before, experimentally, the frequency range for which there is a significant difference in transmission (15.5-17.0 kHz) is narrower than in the numerical results (12.8-16.2 kHz). The difference between the numerical and experimental results might

arise because of a weaker experimental partial bandgap. Discrepancies between the numerical and experimental results especially arise from the viscoelastic behaviour of the 3D-printed PLA, which is also dependent on its geometry [2]. The numerically obtained displacement graph reveals that waveguiding is most effectively achieved at the left and bottom edge of the rim in the partial bandgap. The behaviour can be explained by the directional nature of the partial band gap, which appears only in the Γ-X direction and therefore predominantly attenuates wave propagation along the x- and y-axes. Comparing the transmission of the corner unit cell and the unit cell next to the input in the experimental results reveals that waveguiding occurs from 15.7 to 16.1 kHz and from 16.3 to 16.7 kHz. The experimental results highlight consistent waveguiding throughout this entire frequency range.

7.1.1 Comparison to homogeneous structure

Figure 7.8 shows two homogeneous structures of unit cell configurations used for the waveguiding along the rim metamaterial design. The thin ligament unit cell refers to the unit cell with configuration $r = 9.6$ mm, $w = 1.2$ mm, and $\theta = 0°$. The combination of design parameters $r = 12.0$ mm, $w = 8.0$ mm, and $\theta = 0°$ is referred to as the 8.0 mm thick ligament unit cell. Figure 7.9 plots the transmission of these two homogeneous structures. The homogeneous structure of thin ligament unit cells displays one wide, clear bandgap from Bragg scattering. This full bandgap aligns well with the prediction from the dispersion analysis. However, the first partial bandgap appears narrower and the second partial bandgap broader.

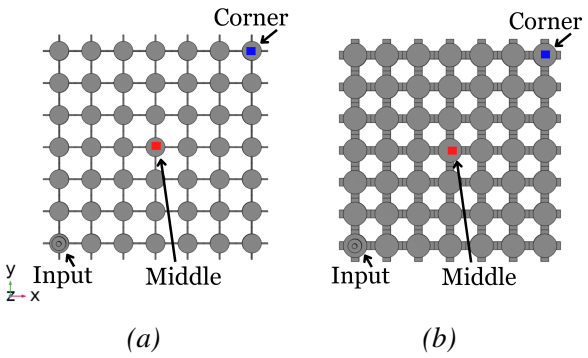

Figure 7.8: Homogeneous structures consisting of (a) thin ligament unit cells and (b) 8.0 mm thick ligament unit cells. The coloured squares indicate where the transmission is measured and correspond with the colours in their respective transmission plots.

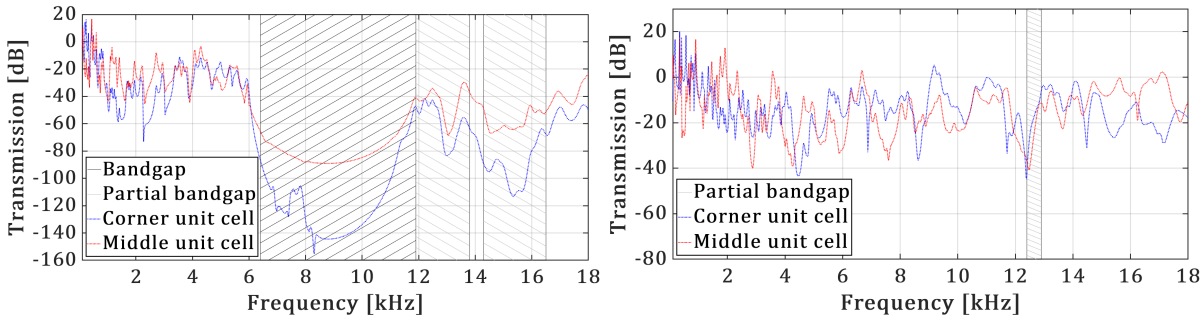

(a) *(b)*

Figure 7.9: Transmission curves of homogeneous structures consisting of (a) thin ligament unit cells and (b) 8.0 mm thick unit cells. The numerically obtained full bandgaps from the dispersion analysis of the unit cell are indicated by the black dashed lines, while the grey dashed lines indicate partial bandgaps.

Figure 7.10 compares the displacement throughout the structures at the same frequencies as in Figure 7.7. Appendix B provides an overview of the maximum displacement obtained in the homogeneous structures at specified frequencies (Table 2).

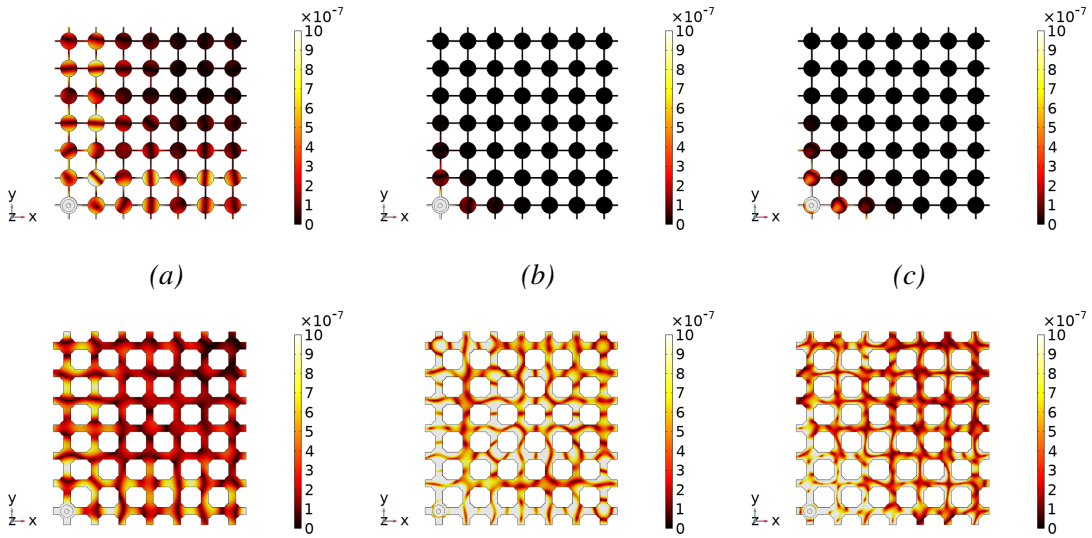

(a) *(b)* *(c)*

(d) *(e)* *(f)*

Figure 7.10: Displacement graphs for the homogeneous structures of unit cell configurations used for the waveguiding along the rim metamaterial. The top row presents the displacement of the thin ligament homogeneous structure at (a) 4.7 kHz, (b) 9.1 kHz, and (c) 14.9 kHz. The bottom row presents the displacement of the 8.0 mm thick ligament homogeneous structure at (d) 4.7 kHz, (e) 9.1 kHz, and (f) 14.9 kHz.

Within both bandgaps, numerically, the difference between the designed metamaterial for waveguiding along the rim and the homogeneous structures built of 8.0 mm thick ligament unit cells can be highlighted. In the first bandgap, at 9.1 kHz, it is evident that overall the metamaterial designed for waveguiding along the rim shows a large difference in the middle of the structure,

where the displacement is visibly lower than along the rim (Figure 7.7). The designed structure has higher wave localisation along the rim, although only comparing the left and the bottom edge highlights similar displacement in the homogeneous structure (Figure 7.10). However, the maximum displacement in the designed metamaterial is more than four times larger than the maximum in the homogeneous structure. In the partial bandgap of the thin ligament unit cells, at 14.9 kHz, the designed metamaterial highlights stronger wave attenuation. The displacement along almost the entire rim in the homogeneous structure is smaller than in the designed metamaterial. The difference in maximum displacement is less significant. Additionally, it should be noted that in the full bandgap, the maximum displacement is more than eleven times as large as in the partial bandgap. Outside any bandgap, at 4.7 kHz for example, the behaviour and the maximum displacement of the homogeneous and designed structure are very similar.

7.2 Waveguiding straight path

Figure 7.11 shows the metamaterial for waveguiding along a straight path. The path consists of complete 10.0 mm thick ligament unit cells. The unit cells connected to the path slightly differ from the inclined ligament unit cells. The ligaments connecting to the thick ligaments have a $0°$ inclination angle to ensure structural integrity. Without this change, the path and the outside would not be connected. All other unit cells around the path have the full inclined ligament configuration. The lower middle unit cell is given the initial displacement of 10^{-6} m. The waves are guided through the path of thick ligament unit cells, and the output is the upper-middle unit cell. The transmission is therefore measured at the output, as this unit cell best represents waveguiding along the path. To investigate the symmetry and the effectiveness of the metamaterial, transmission is measured in four unit cells close to and farther away from the path.

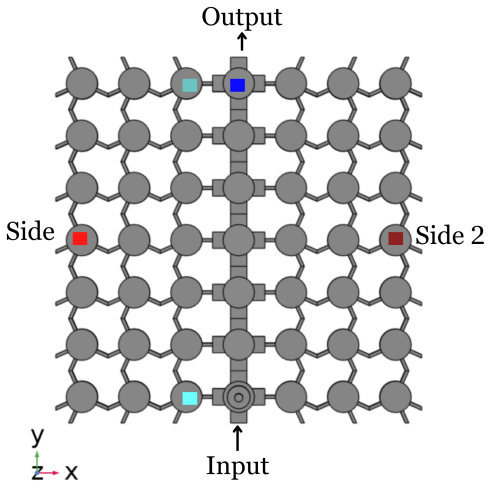

Figure 7.11: The designed metamaterial for waveguiding along a straight path. The coloured squares indicate the points at which the transmission is measured and correspond with the colours in the transmission curves for this structure.

The inclined unit cell has three full out-of-plane bandgaps (6.3-9.5 kHz, 10.5-12.6 kHz, and 14.4-16.6 kHz). The numerically obtained full bandgaps from the dispersion analysis are highlighted in

all transmission curves (Figure 7.12 and 7.13). Waveguiding along the straight path is predicted in the bandgaps. Figure 7.12 highlights that the frequency range from 5.0 kHz onwards is particularly interesting. Especially the first and the third bandgap the transmission at the different unit cells shows large differences. Figure 7.13 compares numerical and experimental results in detailed views from 5.0-11.0 kHz and 11.0-17.0 kHz. Figure 7.14 compares the displacement of the metamaterial at three different frequencies. The first frequency (5.5 kHz) is outside any bandgap, while 8.5 kHz and 15.0 kHz are in the middle of two respective bandgaps of the inclined ligament unit cell. The maximum displacement at each of these frequencies is presented in Appendix B (Table 1). Appendix D Figure 4 presents five more displacement graphs at different frequencies in the first bandgap.

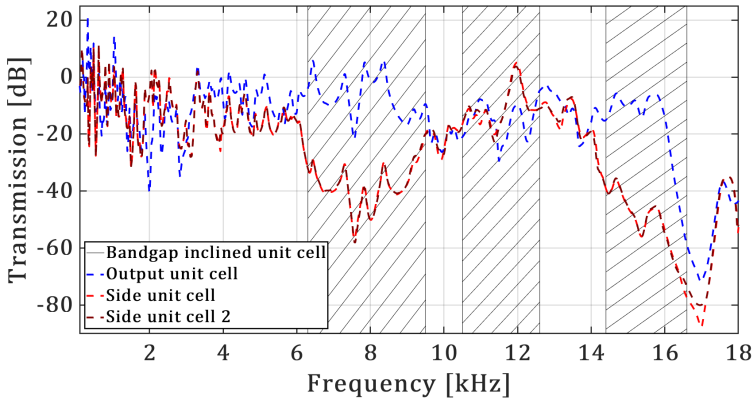

Figure 7.12: Numerical transmission curve for the entire frequency range from 0.1 to 18 kHz. The dashed lines indicate the numerically obtained bandgaps of the inclined ligament unit cell.

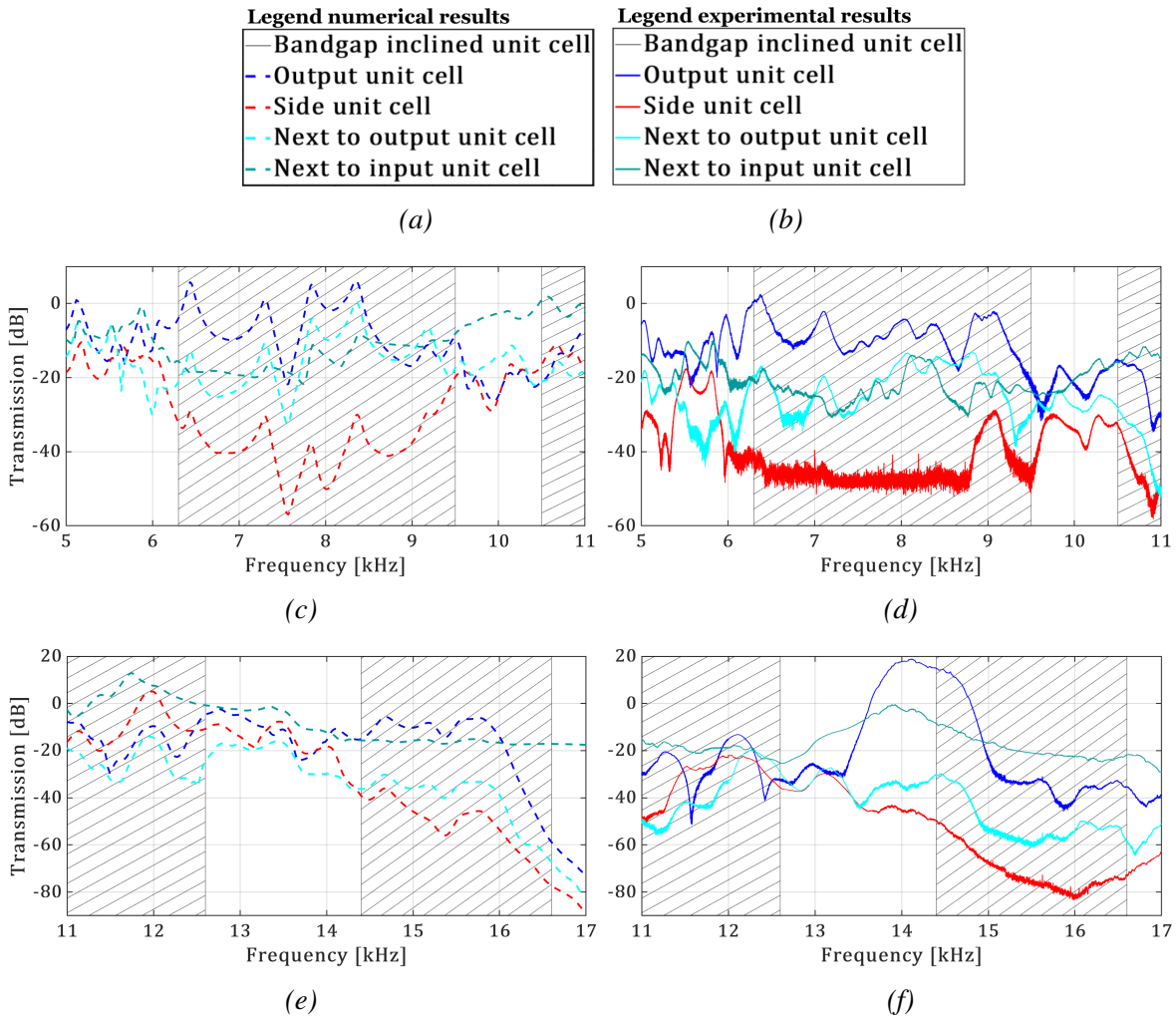

Figure 7.13: Legend for (a) the numerical and (b) the experimental results. Comparison of (c) the numerical transmission curve for 5-11 kHz, (d) the experimental transmission curve for 5-11 kHz, (e) the numerical transmission curve for 11-17 kHz, and (f) the experimental transmission curve for 11-17 kHz.

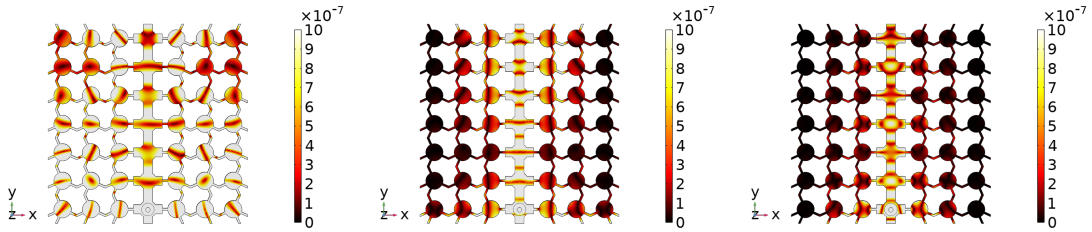

Figure 7.14: Displacement graphs for the waveguiding along a straight path metamaterial at (a) 5.5 kHz, (b) 8.5 kHz, and (c) 15.0 kHz.

The two side unit cells, which are symmetrically located with respect to the path, display almost identical transmission behaviour numerically. Perfect symmetric behaviour is also observed in the displacement graphs. Even the unit cells the furthest off the symmetry line through the middle

of the structure, clearly exhibit the same behaviour as their symmetric located counterpart for all frequencies. The symmetric behaviour is not validated by the experiments, but is used as an assumption for testing only on one side of the middle.

Similar to the metamaterial for waveguiding along the rim, conclusions are based on comparing the output unit cell and the next-to-input unit cell. In general, the unit cell next to the input shows a higher transmission level than the other unit cells off the path. Therefore, it is the best benchmark to indicate successful waveguiding throughout the metamaterial. Numerically, at least a 10.0 dB difference in transmission between the output unit cell and the unit cell next to the input is achieved from 6.3 to 7.5 kHz and from 7.8 to 8.3 kHz in the first bandgap. The experimental results point out a significant transmission difference from 6.2 to 8.2 kHz and from 8.8 to 9.3 kHz (Figure 7.13c and 7.13d). Interestingly, the experiments highlight a broader waveguiding range that matches almost perfectly with the bandgap obtained from dispersion analysis. Numerically, a sharp dip in transmission occurs around 7.6 kHz, which is not visible in the experimental results. Additionally, the drop in transmission, especially for the corner unit cell at the end of the bandgap, is shifted to the left in the numerical results. In general, the transmission behaviour in the first bandgap for the three unit cells off the path aligns between the numerical and experimental results.

In this first bandgap, it becomes visible that waveguiding is achieved over the entire specified frequency range, but that differences occur. Around the end of the first bandgap, the transmission of the unit cell next to the output becomes higher than that of the unit cell next to the input. This is an interesting phenomenon, as it indicates waveguiding is more effective at the beginning of the path than at the end. The behaviour is confirmed by Figure 4b in Appendix D, where waves are attenuated more in the upper unit cells next to the path than next to the input. The rest of Figure 3 (Appendix D) highlights the differences in wave attenuation throughout the bandgap, especially in the unit cells next to the path. Wave attenuation varies among unit cells next to the path, with specific unit cells exhibiting attenuation dependent on the frequency.

Waveguiding is not evident numerically and experimentally in the second bandgap of the inclined ligament structure (Figure 7.12). The behaviour can be attributed to the partial bandgap from 12.1 to 13.4 kHz of the 10.0 mm thick ligament unit cell, although it does not fully interfere with he second bandgap of the inclined ligament structure. The partial bandgap appears to have shifted to a slightly lower and broader frequency range.

In the third bandgap, the numerical transmission of the unit cell next to the input is around 5.0 dB lower than that of the output between 14.5 and 15.9 kHz. Within this frequency range, the transmission at the other unit cells off the path is at least 20.0 dB lower. Therefore, waveguiding is concluded to be successful in this range as well. The displacement graphs show that waveguiding indeed occurs within the third bandgap, but the displacement along the path is lower. Similar behaviour is observed in the experimental results in a lower frequency range. From 13.7 to 14.8 kHz, a transmission difference of at least 5.0 dB is achieved between the output and the next-to-input unit cell (Figure 7.13e and 7.13f). The transmission at the other unit cells off the path is significantly lower than at the output. Interestingly, the transmission of the corner unit

cell highlights a large peak, while the transmission stays relatively stable in the numerical results. This highlights a discrepancy between the numerical model and the experiments. Furthermore, the bandgap appears to have shifted to lower frequencies for the experiments. The same reasons as previously discussed for the structure guiding waves along the rim could hold here. The unit cells next to the path do not comply with the complete inclined ligament configuration, and the dispersion analysis has not been performed on a finite structure.

7.2.1 Comparison to homogeneous structures

Figure 7.15 shows the two homogeneous structures of unit cell configurations used for the metamaterial designed for waveguiding along a straight path. The inclined ligament unit cell is the configuration with parameters $r = 9.6$ mm, $w = 2.0$ mm, and $\theta = 24°$. The 10.0 mm thick ligament unit cell refers to the combination of $r = 9.6$ mm, $w = 10.0$ mm, and $\theta = 0°$. The transmission of these two homogeneous structures is depicted in Figure 7.16. The influence of inertial amplification is visible in the transmission curve of the homogeneous structure made from inclined angle unit cells. The same structure clearly shows alignment with the first and third full numerical bandgaps, although the third bandgap spans to a higher frequency (17.5 kHz) than predicted by the dispersion analysis. The second bandgap, on the other hand, does not appear in the transmission curve. An explanation could be that the bandgaps from dispersion analysis are based on an infinitely periodic structure. A bandgap predicted by dispersion analysis, which is caused by Bragg scattering and highly dependent on the structural periodicity, could deviate in a finite 7x7 structure [26].

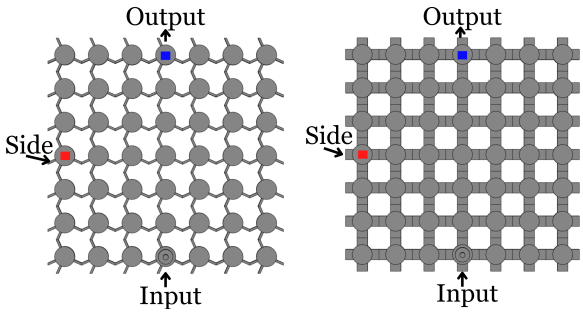

Figure 7.15: Homogeneous structures consisting of (a) inclined ligament unit cells, and (b) 10.0 mm thick ligament unit cells. The coloured squares indicate where the transmission is measured and correspond with the colours in their respective transmission plots.

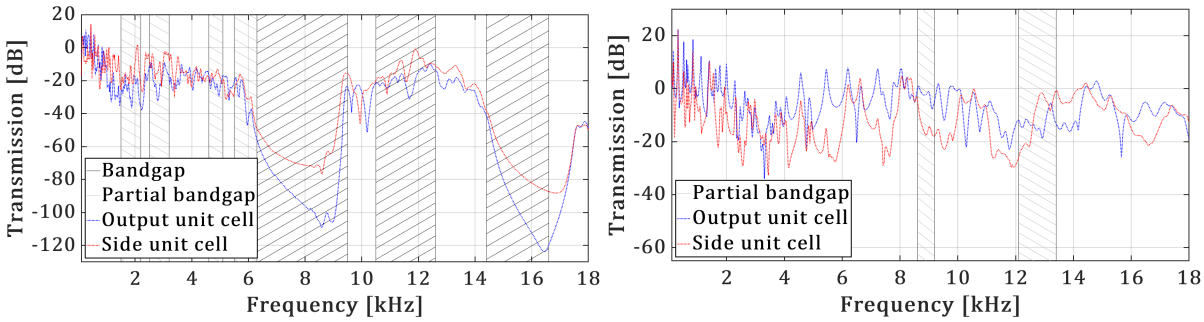

Figure 7.16: Transmission curves of homogeneous structures consisting of (a) inclined ligament unit cells and (b) 10.0 mm thick ligament unit cells. The numerically obtained full bandgaps from the dispersion analysis of the unit cell are indicated by the black dashed lines, while the grey dashed lines indicate partial bandgaps.

Figure 7.17 compares the displacement in the structures at the same three frequencies as in 7.14. The maximum displacement at the given frequencies for these homogeneous structures is presented in Appendix B Table 2.

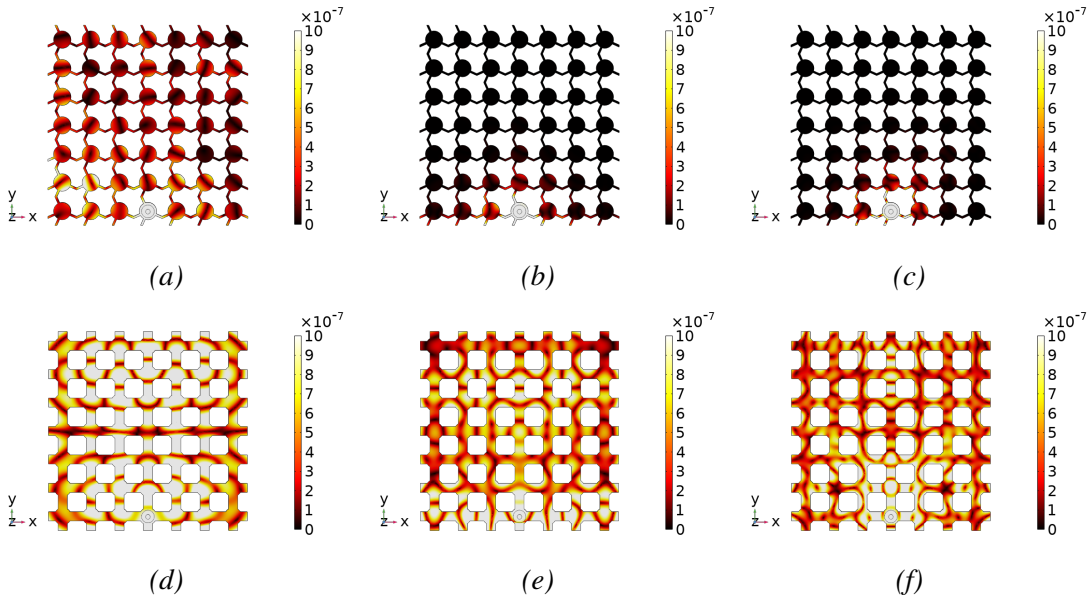

Figure 7.17: Displacement graphs for the homogeneous structures of unit cell configurations used for the waveguiding along a straight path metamaterial. The top row presents the displacement of the inclined ligament homogeneous structure at (a) 5.5 kHz, (b) 8.5 kHz, and (c) 15.0 kHz. The bottom row presents the displacement of the 10.0 mm thick ligament homogeneous structure at (d) 5.5 kHz, (e) 8.5 kHz, and (f) 15.0 kHz.

In general, the transmission curves of the homogenous structures align very well with the numerically obtained full out-of-plane bandgaps from the dispersion analysis. For some structures, discrepancies appear in partial bandgaps. Additionally, some more narrow partial bandgaps appear for some structures. The displacement graphs for the homogeneous structure display

predicted behaviour (Figure 7.10 and 7.17). Close to zero displacement in the entire structure is visible within a full bandgap of their respective unit cells, which highlights wave attenuation. For frequencies apart from (partial) bandgaps, displacement is distributed throughout the entire structure. Furthest away from the excitation, however, less displacement is observed. Different modes for different frequencies also become visible. The homogeneous structures do not display evident waveguiding behaviour. However, in the bandgaps, a clear difference in transmission throughout the structure is observed for the thin ligament and inclined ligament structures. The difference is most likely due to the relative positions of the unit cells with lower transmission, which are located farther from the excitation source.

The behaviour between the metamaterial designed for waveguiding along a straight path and the homogeneous structure with 10.0 mm thick ligament unit cells can be compared (Figure 7.17 and 7.14). The displacement distribution and the maximum displacement are similar outside any bandgap (5.5 kHz). In the first bandgap, at 8.5 kHz, the displacement along the path of the designed structure is visibly larger than in the homogeneous structure. Strong wave attenuation is highlighted, especially along the left and right edges of the structure. The maximum displacement, however, is similar in both structures. A similar comparison holds for the third bandgap of the inclined ligament unit cell. At 15.0 kHz the displacement along the path is more comparable, but waves are strongly attenuated in the designed structure.

Chapter 8 Conclusion

In this study, first, the influence of changing the three design parameters (w, r, θ) on the wave propagation in the unit cell was investigated. Based on the results, two metamaterial designs for waveguiding were be created. One guides the waves along the outer rim, while the other guides the waves along a predefined straight path. Transmission analysis for both structures was conducted numerically and experimentally. The transmission results were compared to the results of the homogeneous structures, consisting of the same unit cells used for the designs, to study the effectiveness of waveguiding in the designs.

It can be concluded from the experiments that waveguiding is achieved in both designed metamaterials. Waves are excellently localised along the predefined paths, proven by a significant transmission difference of at least 10.0 dB between the predefined path and the surrounding region. The metamaterial designed for guiding the waves along the rim achieves waveguiding in the frequency ranges 6.9-9.2 kHz, 15.7-16.1 kHz, and 16.3-16.7 kHz. Numerically, it is observed that the structure exhibits strong wave localisation along the rim, especially in the full bandgap (6.9-9.2). The displacement along the rim significantly increases with respect to the homogeneous structure made of the unit cells along the rim. As predicted, waveguiding is less evident in the partial bandgap (15.7-16.1 kHz, and 16.3-16.7 kHz). Waves are only excellently guided at the edges adjacent to the input, but the overall displacement is not significantly higher than in the homogeneous structure.

The other designed metamaterial enables waveguiding along the predefined straight path in the frequency bands of 6.2–8.2 kHz, 8.8–9.3 kHz, and 13.7–14.8 kHz. Strong wave attenuation in the region outside the path is achieved, but no significant increase in the maximum displacement is observed. In the first bandgap (6.2–8.2 kHz and 8.8–9.3 kHz), wave attenuation next to the path slightly varies with the frequency. From 13.7–14.8 kHz waveguiding is to some degree less effective than in the first bandgap, especially compared to the unit cells next to the path.

Experimental results confirm the validity of the numerical transmission model. However, some discrepancies occur for both metamaterial designs for waveguiding. The frequency ranges over which waveguiding was predicted are shifted slightly down in the experimental results. Moreover, waveguiding within some (partial) bandgaps occurs in a narrower frequency range. Investigating the misalignments could help improve the accuracy of the numerical model. The numerical transmission model also agrees with the dispersion analysis, from which the bandgaps of the unit cells were determined. The differences are explained by the dispersion calculated for an infinite arrangement of unit cells. The behaviour of bandgaps in a structure that consists of different unit cell configurations can also not be completely accurately predicted, since such designs comply even less with the assumption of an infinite arrangement of the same unit cell.

The two metamaterial designs for waveguiding can be further investigated in the future for

applications such as energy harvesting. Firstly, the feasibility of energy harvesting in the frequency ranges over which waveguiding is effective should be considered. Additionally, the precise efficiency should be studied, but for now, the metamaterial that guides waves along the rim appears most efficient for a specific frequency range (6.9-9.2 kHz).

The parametric study results have proven valuable for designing metamaterials for waveguiding. The results can be used to design more metamaterials for wave control in a desired frequency range. This study can act as a starting point for metamaterials designed for wave amplification or wave deviation, for example. Furthermore, waveguiding can be further investigated by predefining a curved or angled path. Depending on the application, different combinations of unit cells might be suitable. Additionally, it is possible to design metamaterials with a different unit cell size than the 32.0 mm adopted in this study. However, it is recommended to choose a unit cell size of the same order of magnitude, as large deviations from the configuration used in this study could result in shifts in the bandgaps.

Bibliography

[1] J. Liu, H. Guo, and T. Wang, "A review of acoustic metamaterials and phononic crystals," *Crystals*, vol. 10, no. 4, p. 305, 2020. DOI: 10.3390/cryst10040305.

[2] A. Krushynska, N. Anerao, M. Badillo Ävila, M. Stokroos, and M. Acuautla, "Arbitrary-curved waveguiding and broadband attenuation in additively manufactured lattice phononic media," English, *Materials design*, vol. 205, Jul. 2021, ISSN: 0261-3069. DOI: 10.1016/j.matdes.2021.109714.

[3] R. V. Craster and S. Guenneau, *Acoustic Metamaterials: Absorption, Cloaking, Imaging, Time-Modulated Media, and Topological Crystals*, Second. Springer, 2024. DOI: 10.1007/978-3-031-60015-9.

[4] X. Tian, W. Chen, R. Gao, and S. Liu, "Merging bragg and local resonance bandgaps in perforated elastic metamaterials with embedded spiral holes," *Journal of Sound and Vibration*, vol. 500, p. 116 036, 2021. DOI: 10.1016/j.jsv.2021.116036.

[5] Z. Chen, B. Guo, Y. Yang, and C. Cheng, "Metamaterials-based enhanced energy harvesting: A review," *Physica B: Condensed Matter*, vol. 438, pp. 1–8, 2014. DOI: 10.1016/j.physb.2013.12.040.

[6] P. I. Koutsianitis, G. K. Tairidis, G. A. Drosopoulos, and G. E. Stavroulakis, "Conventional and star-shaped auxetic materials for the creation of band gaps," *Archive of Applied Mechanics*, vol. 89, no. 12, pp. 2545–2562, 2019. DOI: 10.1007/s00419-019-01594-1.

[7] M. I. Hussein, M. J. Leamy, and M. Ruzzene, "Dynamics of phononic materials and structures: Historical origins, recent progress, and future outlook," *Applied Mechanics Reviews*, vol. 66, no. 4, May 2014. DOI: 10.1115/1.4026911.

[8] C. Yilmaz, G. M. Hulbert, and N. Kikuchi, "Phononic band gaps induced by inertial amplification in periodic media," *Physical Review B*, vol. 76, no. 5, Aug. 2007. DOI: 10.1103/physrevb.76.054309.

[9] G. Liao, C. Luan, Z. Wang, J. Liu, X. Yao, and J. Fu, "Acoustic metamaterials: A review of theories, structures, fabrication approaches, and applications," *Advanced Materials Technologies*, vol. 6, no. 5, p. 2 000 787, 2021. DOI: doi.org/10.1002/admt.202000787.

[10] A. Krushynska, D. Torrent, A. Aragón, *et al.*, "Emerging topics in nanophononics and elastic, acoustic, and mechanical metamaterials: An overview," English, *Nanophotonics*, vol. 12, no. 4, pp. 659–686, Jan. 2023, ISSN: 2192-8606. DOI: 10.1515/nanoph-2022-0671.

[11] A. Hosseinkhani, F. Ebrahimian, D. Younesian, and A. Moayedizadeh, "Defected meta-lattice structures for the enhanced localized vibrational energy harvesting," *Nano Energy*, vol. 100, p. 107 488, 2022. DOI: 10.1016/j.nanoen.2022.107488.

[12] G. Hu, L. Tang, J. Liang, C. Lan, and R. Das, "Acoustic-elastic metamaterials and phononic crystals for energy harvesting: A review," *Smart Materials and Structures*, vol. 30, no. 8, p. 085 025, 2021. DOI: 10.1088/1361-665X/ac0cbc.

[13] A. Krushynska, S. Janbaz, J. Oh, M. Wegener, and N. Fang, "Fundamentals and applications of metamaterials: Breaking the limits," English, *Applied Physics Letters*, vol. 123, no. 24, Dec. 2023, ISSN: 0003-6951. DOI: 10.1063/5.0189043.

[14] S. Beniwal, R. Bose, and A. Krushynska, "Characterizing dissipative elastic metamaterials produced by additive manufacturing," English, *Journal of Visualized Experiments*, vol. 2024, no. 208, Jun. 2024, Publisher Copyright: © 2024 JoVE Journal of Visualized Experiments., ISSN: 1940-087X. DOI: 10.3791/66898.

[15] H. B. A. Ba'ba'a, "Active elastic metamaterials with equidistant solely resonant bandgaps," *arXiv preprint arXiv:2311.08959*, 2023. DOI: 10.1016/j.mechrescom.2024.104269.

[16] R. Zaccherini, A. Colombi, A. Palermo, H. R. Thomsen, and E. N. Chatzi, "Stress-optimized inertial amplified metastructure with opposite chirality for vibration attenuation," *arXiv preprint arXiv:2111.08594*, 2021. DOI: 10.48550/arXiv.2111.08594.

[17] A. Singh and A. Gupta, "Directional bandgap analysis in phononic crystal with rectangular super cell structure," *International Journal of Mathematical, Engineering and Management Sciences*, vol. 7, no. 3, p. 341, 2022. DOI: 10.33889/IJMEMS.2022.7.3.023.

[18] C. Croënne, E. Lee, H. Hu, and J. Page, "Band gaps in phononic crystals: Generation mechanisms and interaction effects," *AIP Advances*, vol. 1, no. 4, 2011. DOI: 10.1063/1.3675797.

[19] L. Gao, C. Cai, C. M. Mak, X. He, Y. Zou, and D. Wu, "Surface wave attenuation by periodic hollow steel trenches with bragg band gap and local resonance band gap," *Construction and Building Materials*, vol. 356, p. 129 289, 2022. DOI: 10.1016/j.conbuildmat.2022.129289.

[20] F. Casadei, T. Delpero, A. Bergamini, P. Ermanni, and M. Ruzzene, "Piezoelectric resonator arrays for tunable acoustic waveguides and metamaterials," *Journal of Applied Physics*, vol. 112, no. 6, Sep. 2012. DOI: 10.1063/1.4752468.

[21] A. Sridhar, V. G. Kouznetsova, and M. G. Geers, "Homogenization of locally resonant acoustic metamaterials towards an emergent enriched continuum," *Computational Mechanics*, vol. 57, no. 3, pp. 423–435, Feb. 2016. DOI: 10.1007/s00466-015-1254-y.

[22] P. Szymczyk-Ziółkowska, M. B. Łabowska, J. Detyna, I. Michalak, and P. Gruber, "A review of fabrication polymer scaffolds for biomedical applications using additive manufacturing techniques," *Biocybernetics and Biomedical Engineering*, vol. 40, no. 2, pp. 624–638, 2020. DOI: 10.1016/j.bbe.2020.01.015.

[23] BambuLab, *Bambu lab x1c 3d printer*. [Online]. Available: https://eu.store.bambulab.com/en-it/products/x1-carbon?srsltid=AfmBOopF0a_-ze9zOYawHM4OsDa-vTSUsT5oHiUdzBjLsQadDFN95IHX.

[24] Ł. Zgryza, A. Raczyńska, and M. Paśnikowska-Łukaszuk, "Thermovisual measurements of 3d printing of abs and pla filaments," *Advances in Science and Technology Research Journal*, vol. 12, no. 3, pp. 266–271, Sep. 2018. DOI: 10.12913/22998624/94325.

[25] L. D'Alessandro, A. Krushynska, R. Ardito, N. Pugno, and A. Corigliano, "A design strategy to match the band gap of periodic and aperiodic metamaterials," English, *Scientific Reports*, vol. 10, Oct. 2020, ISSN: 2045-2322. DOI: 10.1038/s41598-020-73299-3.

[26] V. Zega, L. Pertoldi, T. Zandrini, R. Osellame, C. Comi, and A. Corigliano, "Microstructured phononic crystal isolates from ultrasonic mechanical vibrations," *Applied sciences*, vol. 12, no. 5, p. 2499, 2022. DOI: 10.3390/app12052499.

Appendix

A. Dispersion curve

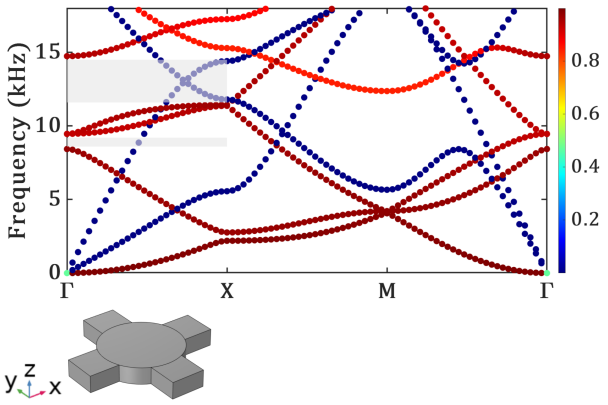

Figure 1: Dispersion curve for unit cell with configuration $w = 8$ *mm,* $r = 9.6$ *mm, and* $\theta = 0°$*. The light grey areas indicate partial out-of-plane bandgaps.*

B Maximum displacement

Designed structure	Frequency [kHz]	Maximum displacement [m]
Waveguiding along outer rim	4.7	$1.51213 \cdot 10^{-6}$
	9.1	$6.67421 \cdot 10^{-5}$
	14.9	$5.61044 \cdot 10^{-6}$
Waveguiding along straight path	5.5	$4.24691 \cdot 10^{-6}$
	8.5	$1.67442 \cdot 10^{-5}$
	15.0	$2.79051 \cdot 10^{-6}$

Table 1: Maximum displacement for the designed structures at frequencies from the presented displacement graphs (Figure 7.7 and 7.14).

Homogeneous structure	Frequency [kHz]	Maximum displacement [m]
Thin ligament unit cells	4.7	$1.59896 \cdot 10^{-6}$
	9.1	$2.34321 \cdot 10^{-5}$
	14.9	$7.13288 \cdot 10^{-6}$
8.0 mm thick ligament unit cells	4.7	$1.68872 \cdot 10^{-6}$
	9.1	$1.40352 \cdot 10^{-5}$
	14.9	$3.49772 \cdot 10^{-6}$
Inclined ligament unit cells	5.5	$1.8373 \cdot 10^{-6}$
	8.5	$8.42057 \cdot 10^{-6}$
	15.0	$1.87641 \cdot 10^{-6}$
10.0 mm thick ligament unit cells	5.5	$3.91289 \cdot 10^{-6}$
	8.5	$1.33563 \cdot 10^{-5}$
	15.0	$3.14155 \cdot 10^{-6}$

Table 2: Maximum displacement for the homogeneous structures at frequencies from the presented displacement graphs (Figure 7.10 and 7.17).

C Alternative waveguiding outer rim design

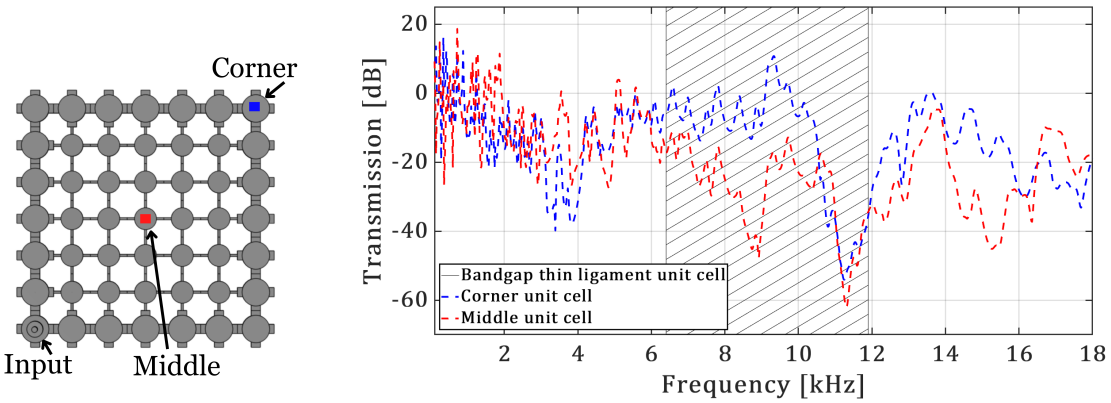

(a) *(b)*

Figure 2: (a) The designed metamaterial with full thick ligament unit cells along the rim. The coloured squares indicate the points at which the transmission is measured and correspond with the colours in (b) the transmission curve for this structure.

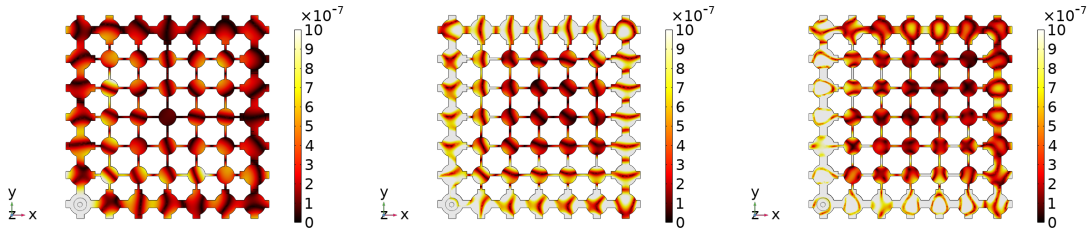

(a) *(b)* *(c)*

Figure 3: Displacement graphs of the metamaterial designed for waveguiding along the rim with four thick ligaments at (a) 4.7 kHz, (b) 9.1 kHz, and (c) 14.9 kHz.

D Waveguiding along path in first bandgap

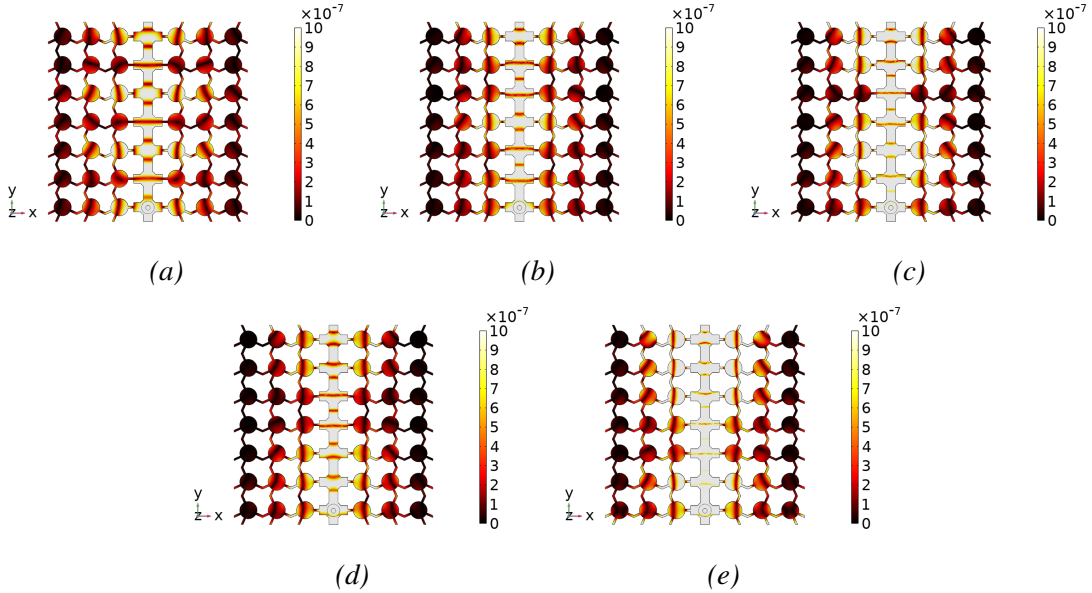

Figure 4: Displacement graphs for the waveguiding along a straight path metamaterial at (a) 6.5 kHz, (b) 7.3 kHz, (c) 7.8 kHz, (d) 8.0 kHz, and (e) 8.4 kHz.